

Cite this: *Anal. Methods*, 2025, 17, 2161

## An Ag-nanoplate decorated cavity-nanorod array SERS substrate for trace detection of PCB-77†

Jinran Chen,<sup>abc</sup> Xiurui Ke,<sup>ac</sup> Zhou Zhou,<sup>d</sup> Wenqi Ye,<sup>id</sup>\*<sup>ac</sup> Hong Liu,<sup>id</sup><sup>ac</sup> Wei Zhang<sup>ac</sup> and Xiaohong Liu<sup>\*e</sup>

We report the fabrication of a substrate with cavity-nanorods and decorated with Ag-nanoplates (C-NR@Ag). The cavities on the substrate are formed by metal assistant chemical etching, and the Ag-nanoplates in the cavities by galvanic cell deposition enhance the SERS performance effectively. Analytes in solution are adsorbed on Ag-nanoplates and located in hot spots, which enhance the SERS performance effectively. The enhancement factor of the Ag-nanoplates decorated on nanorod cavities is calculated to be  $3.6 \times 10^6$ , which is about 3 fold higher than that on the nanorods. The C-NR@Ag substrate is able to detect polychlorinated biphenyls (PCBs) with the lower limit of detection at  $1.0 \times 10^{-12}$  M. Additionally, due to the semi-volatile nature of PCB-77, the lower limit of detection of the C-NR@Ag substrate for PCB-77 was  $1.0 \times 10^{-11}$  M by the non-contact collection method. These results present a novel approach towards enhancing SERS performance and facilitating the rapid detection of PCB-77.

Received 5th January 2025  
Accepted 6th February 2025

DOI: 10.1039/d5ay00025d

rsc.li/methods

### Introduction

3,3',4,4'-Tetrachlorinated biphenyl (PCB-77) is a dioxin-like compound with high toxicity, bioaccumulation, and migration.<sup>1</sup> Because PCB-77 is difficult to degrade in nature, it is gradually accumulated in the soil and washed into streams and rivers, eventually making a serious impact on human health and the ecological environment. The Stockholm convention required global control on PCBs, and the International Agency for Research on Cancer listed PCBs as Class 1A carcinogens in 2016.<sup>2</sup> The "Surface Water Environmental Quality Standard" domestic and overseas is about  $1.0 \times 10^{-11}$  M, and therefore the trace detection method for PCB-77 is required. The traditional analytical methods to detect PCBs include chromatography,<sup>3-5</sup> immunoassay,<sup>6-8</sup> and spectroscopy.<sup>9-11</sup> Chromatography requires multi-step pretreatment with low efficiency.<sup>12</sup> The immunological method is highly specific and sensitive but with the potential for false positives.<sup>6</sup> Most methods can detect PCBs near  $10^{-11}$  M to meet the requirement.<sup>13</sup> Nowadays detection sensors have become prevalent. Although the LOD of PCBs is as

low as  $10^{-15}$  M, pretreatment procedures<sup>14,15</sup> show the complexity of these methods. However, the cost of the sensors is higher. The SERS substrates exhibit an LOD of  $10^{-11}$  M for PCBs at low cost without pretreatment, indicating the potential of SERS detection.<sup>16,17</sup>

The SERS performance is majorly driven by electromagnetic field enhancement at the nanoscale "hot spots" between metal nanoparticles, which is attributed to localized surface plasmon resonance (LSPR).<sup>18</sup> LSPR is generated in the nanogaps of metal nanoparticles and depends on the size and morphology of metal nanoparticles and the gaps between nanoparticles. The strategy of forming hot spots is different in SERS-active colloidal systems and chip-based substrates. In the SERS-active colloidal system, formed through the random aggregation of nanoparticles, high-density hot spots could locate analytes and enhance SERS performance.<sup>19-21</sup> The chemical mechanism is another important reason for Raman enhancement, based on charge transfer between molecules and substrates. Therefore, strategies for the substrate to transfer electrons, such as temperature control<sup>22</sup> and regulating polarization,<sup>23</sup> are needed to improve SERS activity. On a chip-based substrate, hot spots with reproducibility are formed by nanoparticles, which are arranged or decorated on the substrate.<sup>24-26</sup> Substrates such as commercial Klarite chips have advantages in manufacturing and usage. The performance of the SERS substrate relies on hot spots with high-density and reproducibility. Thus, hot spots formed on the substrate with uniformity and reproducibility have been the focus of the SERS substrate.<sup>27,28</sup> Sputtering was a general method to form hot spots and many substrates showed significant reliability and reproducibility. However, the distribution of sputtering hot spots was determined by the

<sup>a</sup>Chongqing Institute of Green and Intelligent Technology, Chinese Academy of Sciences, Chongqing 400714, P. R. China. E-mail: yewenqi@cigit.ac.cn

<sup>b</sup>Chongqing Jiaotong University, Chongqing, 400074, P. R. China

<sup>c</sup>Chongqing School, University of Chinese Academy of Sciences (UCAS Chongqing), Chongqing 400714, P. R. China

<sup>d</sup>The University of Manchester, Department of Materials, Oxford Road, Manchester M13 9PL, UK

<sup>e</sup>National University of Singapore (Chongqing) Research Institute, Chongqing, 401123, P. R. China. E-mail: xiaohong.liu@nusricq.cn

† Electronic supplementary information (ESI) available. See DOI: <https://doi.org/10.1039/d5ay00025d>

morphology of the substrate, and it can be adjusted to be uniform by electrochemical or thermal annealing.<sup>29,30</sup> Thermal annealing was influenced by factors such as temperature and time, leading to issues with non-uniformity in hot spot formation. Electrodeposition is a widely employed technique for achieving high uniformity in the deposition of metallic nanoparticles onto substrates by reducing metal ions.

Galvanic cell deposition, as an electrochemical approach, offers the advantages of not requiring an electric current and forming no residues in metal nanostructures.<sup>31–34</sup> In this process, nanoparticles are gradually produced, with the size of the nanoparticles increasing and the gaps between them narrowing down, and hot spots are located in gaps. However, extending the deposition time will cause the nanoparticles to become larger and decrease the hot spots instead, forming irregular hot spots, which may reduce the SERS effect. Early studies<sup>34–36</sup> showed that Ag nanoplate arrays by galvanic cell deposition had potential in trace detection, and Ag nanoparticles had a high sensitivity for PCB-77 detection.<sup>36–38</sup> Tan *et al.*<sup>39</sup> showed that Ag nanoplates exhibit a 3D shape, which proves that the reason why Ag nanoplates can offer more hot spots is multidimension rather than the rough surface. Furthermore, Chang *et al.*<sup>40</sup> offered a reliable method to shape 3D structures on silicon wafer. In this case, increasing the specific surface area in order to allow more Ag-nanoplates to form 3D structures is a good way to increase hot spots.

In this paper, we fabricate an array-based substrate by a simple method, to increase the specific surface area of the substrate by forming cavities on the surface of the nanorod, and deposit Ag-nanoplates on the substrate surface by galvanic cell deposition. And the performance of the SERS substrate is improved, which can be proven in trace detection of PCB-77. Also, the substrate can detect PCB-77 molecules in the air.

## Experimental

### Materials

Monodisperse silica microspheres (SiO<sub>2</sub>, 500 nm, 2.5 wt%) were purchased from Macklin. Cetyltrimethylammonium bromide (CTAB, ≥99.7%) was purchased from Sigma-Aldrich. Rhodamine 6G (R6G, 99%), 3,3',4,4'-tetrachlorobiphenyl (PCB-77, 99%) and silver nitrate (AgNO<sub>3</sub>, 99%) were purchased from Aladdin. One-side polished p-type (100)-oriented silicon wafer without an oxide layer was purchased from Zhongnuoxincai Technology Co. Ltd (Beijing). Ethanol and methanol were purchased from Knowles Agents Co. Ltd (Chengdu). Hydrofluoric acid (HF, 49%) and hydrogen peroxide (H<sub>2</sub>O<sub>2</sub>, 30%) were purchased from Chengdu Kelong Chemical. Sulfuric acid (H<sub>2</sub>SO<sub>4</sub>, 98%) and nitric acid were purchased from Chuandong Chemical. Deionized water (DI) was purified by Molecular@ΣH<sub>2</sub>O systems.

### Apparatuses

An ultrasonic cleaner (Ningbo Scientz Biotechnology, SB-5200 DTDN, China) was used to clean the wafer and mix the solution. A thin film sputtering system (Alliance concept, DP650,

France) was utilized to sputter Au nanoparticles. A Schottky field emission scanning electron microscope (FESEM, JEOL, JSM-7800F, Japan) was used for morphology observation of the substrate. A confocal microscope Raman spectrometer (Renishaw, InVia Rerlex, The UK) was used to collect SERS spectra. A reactive ion etching machine (Beijing Plasma Technology, Filmlab-R100, China) was used to etch the wafer.

### Fabrication of the cavity-nanorod@Ag substrate

1 × 1 cm<sup>2</sup> silicon wafer was washed with DI water and ethanol in sequence, and then dried in an oven before being soaked in piranha solution with H<sub>2</sub>SO<sub>4</sub> : H<sub>2</sub>O<sub>2</sub> = 7 : 3 (V/V) for 12 h to clean thoroughly followed by washing in DI water to obtain a hydrophilic surface. The monodisperse SiO<sub>2</sub> nanospheres were cleaned with ethanol and then dispersed in ethanol to no flocculation using an ultrasonic bath. When the dispersion came into contact with the water surface, the SiO<sub>2</sub> nanospheres spread outward due to the presence of ethanol. With the assistance of CTAB in DI water, these nanospheres self-assembled on the surface of the water, forming a closely packed monolayer. This monolayer could then be easily transferred onto the surface of a cleaned silicon wafer (Fig. 1a). Subsequently, a nanorod array (NR) structure could be created on the wafer using reactive ion etching (RIE), utilizing the closely packed monolayer of SiO<sub>2</sub> nanospheres as a mask (Fig. 1b). The SF<sub>6</sub> and O<sub>2</sub> plasma treatment was utilized to etch the wafer with a close-packed monolayer pattern in the RIE machine vacuum chamber. The cavity structure was formed by metal-assisted chemical etching (MACE) on the nanorod arrays (Fig. 1c), which was performed in two steps: depositing Ag and etching silicon with Ag and H<sub>2</sub>O<sub>2</sub>.<sup>41</sup> The deposition solution used in step one was mixed with equal volumes of AgNO<sub>3</sub> and HF and the etching solution used in step two was mixed with equal volumes of H<sub>2</sub>O<sub>2</sub> and HF. The cavity-nanorod (C-NR) structure (Fig. 1d) was obtained after the Ag particles deposited were removed by soaking in high-concentration nitric acid for 1 h. Au nanoparticles were sputtered onto the C-NR structure to improve conductivity and acted as nuclei in galvanic cell reduction subsequently. The cavity-nanorod@Ag (C-NR@Ag) substrate (Fig. 1e) was achieved through galvanic cell deposition which was modified by the time of deposition.

### SERS measurements

The SERS activity of the substrate was detected using the R6G solution (10<sup>-11</sup> M), the uniformity of the substrate was detected using the *p*-ATP solution (10<sup>-4</sup> M), and the pollutant detection ability of the substrate was detected using the PCB-77 solution (10<sup>-12</sup> M).

For Raman analysis, 30 μL R6G solution was dropped onto the Si wafer and C-NR@Ag substrate. Raman signals were collected on the surface of these samples after the evaporation and averaged from three different points. The homogeneity of the SERS signals was determined by point-by-point Raman mapping over an area of 20 μm × 20 μm, using a step size of 2 μm and a laser spot of diameter 2 μm.



Fig. 1 Schematic of the C-NR@Ag substrate preparation process. (a) SiO<sub>2</sub> microspheres on the substrate surface; (b) the nanorod structure formed by RIE; (c) the cavity-nanorod structure formed by MACE; (d) gold film on the substrate; (e) silver plates formed by galvanic cell deposition.

The diode laser used in this system had wavelengths of 532 nm and 785 nm. A 532 nm laser was used in the detection of R6G with the power attenuated to 0.5% (the original power of 50 mW). A 785 nm laser was used in the detection of *p*-ATP with the power attenuated to 0.1% (the original power of 300 mW). All spectra were collected from 600 cm<sup>-1</sup> to 1700 cm<sup>-1</sup>, with the exposure time at 10 s, the accumulation at 1, and the objective lens at 50×.

### Data processing

All spectra were collected by Renishaw WiRE 3.4 software. And the Raman shift and intensity data were fitted using the Gauss-Lorentz method. The Raman mapping curve was collected in a signal-to-baseline mode.

### Electric field simulation

The electric field distribution of the model was obtained by simulation using COMSOL Multiphysics with the incident laser wavelength at 785 nm. The enhancement factor was calculated

as  $|E|^4$  when the incident strength was  $E = 1V/m$  based on the electromagnetic field mechanism.

## Results and discussion

### Optimization and characterization

The C-NR@Ag substrate was fabricated by RIE, MACE, and galvanic cell reduction (Fig. 1). SiO<sub>2</sub> microspheres were compacted hexagonally on the DI water, and were transferred to the silicon wafer in the same arrangement. The silicon wafer with SiO<sub>2</sub> microspheres (Fig. 1a) was etched by RIE, and the periodic NR structure with height at about 500 nm (Fig. 1b) was constructed using SiO<sub>2</sub> microspheres as the mask. The C-NR structure (Fig. 1c) was formed by the MACE process which can be divided into two steps. Step one was the reduction of Ag<sup>+</sup> to Ag caused by Si-H bonds which were formed between the silicon and HF in the solution. When electrons were transferred from Si-H bonds to Ag<sup>+</sup>, Ag<sup>+</sup> is reduced to Ag and attached to the NR surface. In step two, H<sub>2</sub>O<sub>2</sub> was reduced generating H<sub>2</sub>, silicon was oxidized leaving cavities on the NR surface, and

electrons were transferred between them by Ag. The reaction formula is:



The cavity structure can be adjusted by the amount of Ag particles reduced in step one and etching time in step two. To explore the impact of these factors, an orthogonal test (Table S1†) was designed and analysed by extremum difference analysis (Table S2†) according to the SERS performance of the nine C-NR structures (Fig. 2b).

To evaluate the SERS performance of the NR structure substrates, Au nanoparticles were sputtered onto the surface of the structure. Different amounts of Au nanoparticles were sputtered, and their effects on the structure were compared (Fig. S1†). It was found that sputtering 5 nm Au nanoparticles had a minimal impact on the structure, and thus this amount was chosen for further SERS detection on the substrates. The SERS performance of the NR structure substrates was assessed using an orthogonal test. Among the tested structures, the No. 8 structure exhibited the best SERS performance. Morphological analysis of the different C-NR structures in the orthogonal test (Fig. S2†) revealed that as the deposition time and the concentration of AgNO<sub>3</sub> increased, the amount of Ag particles on the surface of the nanorods gradually increased, and the etching area increased. And the sputtering Au nanoparticles had more area to attach, increasing the density of hot spots. That's the reason why the structure formed with a high concentration of AgNO<sub>3</sub> and a long deposition time showed better SERS performance. However, the large amount of Ag particles could cover the surface of the NR structure and reduce the etching area. Therefore, the best SERS performance was achieved on the structure formed by the AgNO<sub>3</sub> concentration of  $10 \times 10^{-3} \text{ mol L}^{-1}$ , deposition time of 3 min, and etching time of 3 min. By analysing the characteristic peak of R6G in Table S2,† the most critical factor in the orthogonal test

was the concentration of AgNO<sub>3</sub>, followed by deposition time and etching time.

To explore whether the Ag-nanoplates could be deposited uniformly on the structure without Au nanoparticles on the surface, the uniformity of the Ag-nanoplates on the structure with or without Au nanoparticles was compared (Fig. S3†). The EDS (energy dispersive spectrometer) scanning illustrated that Ag nanoplates were distributed uniformly on the NR structure with the Au-sputtered substrate, while Ag nanoplates were irregularly distributed on the surface of the non-Au-sputtered substrate. The result confirmed that the Ag-nanoplates on the structure with Au nanoparticles were assembled uniformly. Then the Ag-nanoplates were decorated on the structure with 5 nm Au nanoparticles by galvanic cell deposition to form the C-NR@Ag substrate. The morphology of different substrates (Fig. S4†) at 5 min, 10 min, and 15 min illustrated that the Ag-nanoplates grew gradually and covered the whole surface of the C-NR structure as the deposition time prolonged. To confirm the deposition time to fabricate the substrate, the SERS performance of the substrates at different deposition times was measured, and the results (Fig. 3a) illustrated that the substrate decorated with Ag-nanoplates in 10 min showed the best SERS performance. The SERS performance of the substrate depends on the size of Ag-nanoplates and the nanogaps between them. With the increase of the deposition time, Ag-nanoplates grew and the nanogaps between Ag-nanoplates decreased. Due to the disordered growth of the Ag-nanoplates, the nanogaps were formed between Ag-nanoplates and still existed even in contact (Fig. S5†), which could be the reason for the enhancement of SERS.

To prove that the SERS performance was impacted by Ag-nanoplates and cavities, the SERS performance of substrates with the NR structure, NR@Ag structure, C-NR structure, and C-NR@Ag structure was measured using the probe molecule. The results (Fig. 3b) illustrated that the SERS performance of C-NR@Ag was better than that of NR, NR@Ag, and C-NR, which

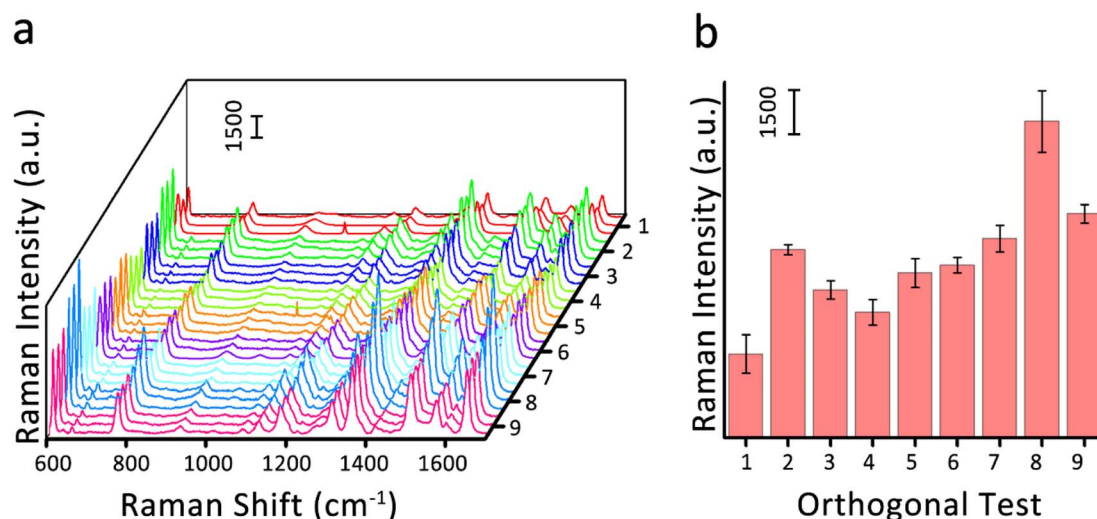


Fig. 2 (a) Raman spectra of substrates in an orthogonal test probing  $10^{-6}$  M R6G. (b) The Raman performance of substrates, using the characteristic peak intensity of  $611 \text{ cm}^{-1}$  based on (a). The error bar was calculated by three replicate determinations.



Fig. 3 (a) Raman spectra of these substrates detecting  $1.0 \times 10^{-6}$  M R6G. (b) Raman spectra of different substrates detecting  $1.0 \times 10^{-6}$  M R6G.

showed the superiority of Ag-nanoplates and cavities. The performance of different substrates was average values of multiple repeat measurements (Fig. S6<sup>†</sup>).

#### Uniformity and reproducibility of the C-NR@Ag substrate

The uniformity and reproducibility of C-NR@Ag were detected by the distribution of Ag-nanoplates and the Raman intensity of probe molecules on the substrate. The EDS (energy dispersive spectrometer) image (Fig. S7<sup>†</sup>) shows that the distribution of silver on the substrate surface was uniform. *p*-ATP can form a bond with Ag and be detected, the enhanced signal is attributed to the localization of the bond at hot spots. Therefore, the uniformity of hot spots on the substrate surface was confirmed by the characteristic peak of the probe molecule. The Raman

intensity of the characteristic peak (Fig. 4a) was obtained to indicate the uniformity of the substrate, and the intensity varied from  $3.5 \times 10^4$  to  $4.2 \times 10^4$ . Five points were selected from each of the four areas top, bottom, left, and right of the plane, and a total of 20 points were detected, and the RSD (relative standard deviation) of 20 points (Fig. S8<sup>†</sup>) was 2.8%. The Raman spectra of four corners and the centre of each substrate from four batches (Fig. S9<sup>†</sup>) were obtained for reproducibility. The Raman intensity of the characteristic peak (Fig. 4b) was analyzed, revealing that the substrates from the four batches exhibited good repeatability, with an RSD of 3.3%. Based on the characterization and analysis mentioned above, it can be concluded that the C-NR@Ag substrate is an ordered array substrate, with consistent and reproducible performance across

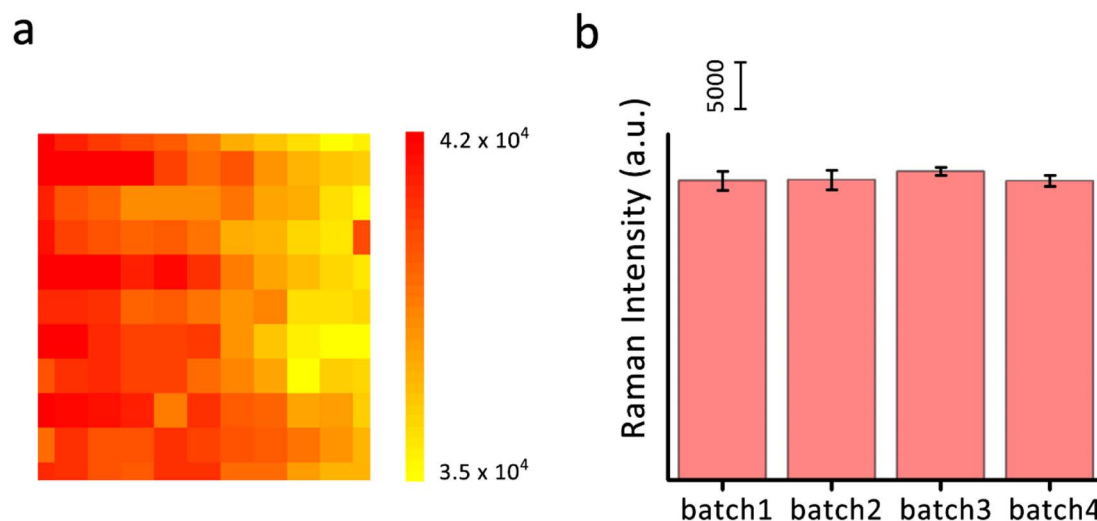


Fig. 4 (a) The uniformity of the substrate using the characteristic peak intensity of  $1078 \text{ cm}^{-1}$ . (b) The reproducibility of the substrate using the characteristic peak intensity of  $1078 \text{ cm}^{-1}$  based on the Raman spectra in Fig. S9.<sup>†</sup>

different batches. SERS spectra were obtained on the substrate with good uniformity and reproducibility.

### SERS activity of the C-NR@Ag substrate

R6G is usually used as a probe molecule to evaluate the SERS activity of the substrate. The SERS detection results (Fig. 5a) showed that the lower limit of detection of R6G on the substrate was  $1.0 \times 10^{-11}$  M. The Raman intensity at  $611 \text{ cm}^{-1}$  is linearly related to the R6G concentration ( $10^{-7}$  to  $10^{-11}$  M), with a correlation coefficient ( $R^2$ ) of 0.93 (Fig. 5b). The enhancement factor (EF) was usually used to evaluate the SERS activity of a substrate, and calculated using the formula:

$$EF = \frac{I_{\text{SERS}}/N_{\text{SERS}}}{I_{\text{Raman}}/N_{\text{Raman}}}$$

The Raman characteristic peak intensity at  $611 \text{ cm}^{-1}$  was used to obtain the EF for the C-NR@Ag substrate, using a cleaned silicon wafer as the reference substrate, where  $I_{\text{SERS}}$  and  $I_{\text{Raman}}$  are the Raman intensities of the samples on the

silicon wafer and C-NR@Ag substrate under the corresponding detection modes.  $N_{\text{SERS}}$  and  $N_{\text{Raman}}$  are the numbers of adsorbed R6G molecules, which are excited by the laser on the silicon wafer and C-NR@Ag substrate. The EF of the C-NR@Ag substrate can reach  $3.6 \times 10^6$ .

The electric field simulation analysis of the substrate was carried out, and the two-dimensional electric field distribution of the model was obtained by COMSOL Multiphysics. The enhancement factor EF of the simulation model can be calculated by the following equation:

$$EF = |E_{(r,\omega)}|^4$$

### Detection of PCB-77

As a dioxin-like PCB, PCB-77 can cause significant damage to the environment and human health due to toxicity. Although SERS substrates have been developed, the lower limit of detection for PCB-77 on most substrates is typically around  $10^{-9}$  M, which falls short of meeting the required Quality Standards.



Fig. 5 (a) SERS activity of the substrate using the R6G solution with concentrations ranging from  $10^{-7}$  to  $10^{-11}$  M. (b) Correlation between the log–log plot of  $I_{611}$  and  $C_{\text{R6G}}$ . The error bar was obtained by three replicate determinations based on the Raman spectra in (a). (c) The electric field simulation of the C-NR substrate. (d) The electric field simulation of the C-NR@Ag substrate.

The trace detection of PCB-77 with high sensitivity is crucial. The PCB-77 solution was diluted in the methanol solution with DI water, so PCB-77 molecules in water were only considered when performing density functional theory (DFT) calculations to analyse vibrational modes. Characteristic peaks of PCBs can be determined by DFT in theoretical calculation and the relevant information reported in the literature. The characteristic peaks of PCBs are seen at  $1290\text{ cm}^{-1}$  (biphenyl C–C bridge stretching of the aromatic ring) and  $1608\text{ cm}^{-1}$  (stretching mode of the aromatic ring).<sup>37,42,43</sup> As shown in Fig. S10,† the results of DFT are in good agreement with the experimental spectra. The deviation in positions of  $1608\text{ cm}^{-1}$  and  $1290\text{ cm}^{-1}$  between DFT-calculated and experimentally detected Raman spectra could arise from the laser power being maintained at 1% during measurements. The Raman intensity of PCB-77 decreased with the decrease of PCB-77 concentrations (Fig. 6a), and Fig. 6b shows the linear relation of the Raman intensity and the logarithmic concentration of PCB-77 ( $1608\text{ cm}^{-1}$ ). The  $R^2$  of linear relation was 0.99 and the lower limit of detection of the C-NR@Ag substrate for PCB-77 was  $1.0 \times 10^{-12}\text{ M}$  which was lower than that of many traditional methods,<sup>16</sup> indicating trace detection of PCB-77 on the C-NR@Ag substrate.

#### Non-contact collection and rapid detection of PCB-77

When using the SERS substrate to detect the PCB-77 solution, the solution was dripping on the surface of the C-NR@Ag substrate and diffused, forming an area to be detected. The PCB-77 molecules presented an uneven deposition state under the “coffee-ring” effect, which makes it difficult to determine the detection area. Furthermore, due to the semi-volatile characteristics of

PCBs, the PCB-77 molecules would diffuse into the air, leaving fewer molecules which made detection more difficult.

Volatile PCB-77 molecules are released from water into the air where they slowly disperse and accumulate. At higher temperature and lower air pressure, the motion of molecules intensifies, which accelerates the diffusion rate of PCB-77. Not only does the degree of diffusion of molecules from water to air increase, but the distribution of molecules in the air is also more uniform. As these PCB-77 molecules float in the air, they encounter Ag-nanoplates on the substrate. Ag-nanoplates provide an ideal attachment platform for PCB-77 molecules. In addition, since the molecules are in direct contact with the silver nanosheets, they attach uniformly to the surface of the Ag-nanoplates and are not affected by liquid evaporation, effectively avoiding the coffee-ring effect.

PCB-77 at a concentration of  $10^{-5}\text{ M}$  was collected by the C-NR@Ag substrate and 49 points were selected within a  $3\text{ mm} \times 3\text{ mm}$  area with a step size of  $0.5\text{ mm}$  for Raman spectroscopy measurements. A mapping image based on the intensity of characteristic peaks at  $1608\text{ cm}^{-1}$  is created (Fig. S11†), showing peak intensities ranging from  $8 \times 10^3$  to  $1.2 \times 10^4$ , indicating that the distribution of PCB-77 molecules on the substrate is uniform. And the spectra from 10 different positions on the substrate surface are shown in Fig. 7a. The Raman intensity of the characteristic peak (Fig. 7b) illustrated that the collection of PCB-77 on the substrate was in good uniformity with RSD at 5.89%. The lower limit of detection for PCB-77 on the C-NR@Ag substrate was  $1.0 \times 10^{-11}\text{ M}$  by the non-contact collection method, and the  $R^2$  of linear relation (Fig. 7d) was 0.99, indicating that the semi-volatile of PCB-77 can be used as a trace detection strategy on the C-NR@Ag substrate.

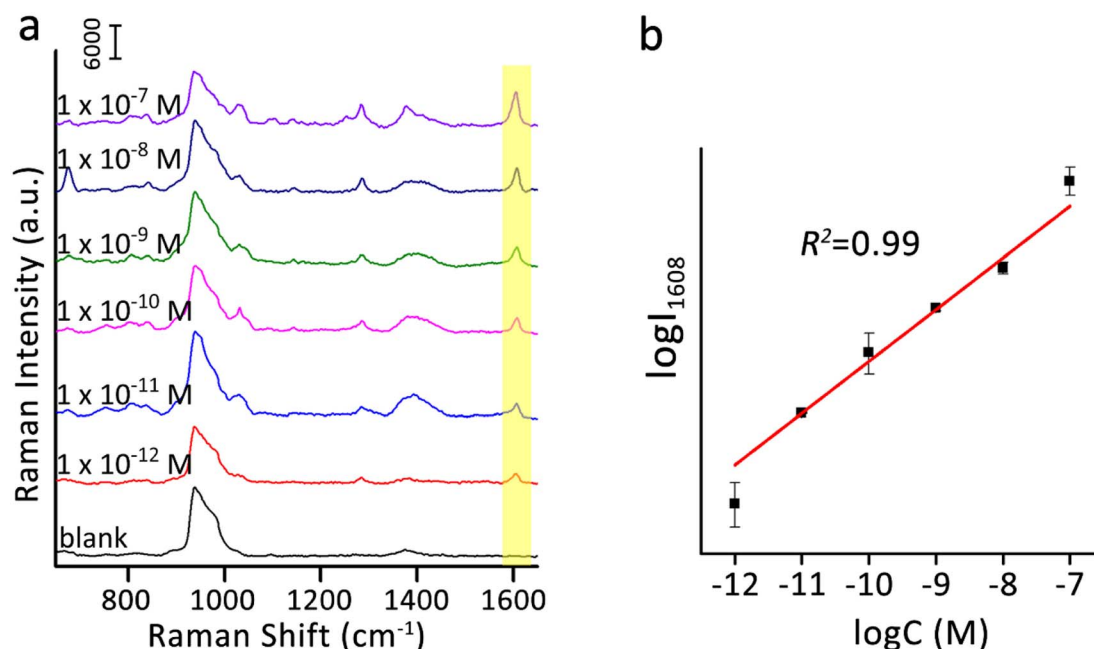


Fig. 6 (a)  $10^{-7}$  to  $10^{-12}\text{ M}$  concentrations of PCB-77 are detected on the C-NR@Ag substrate. (b) Correlation between the log–log plot of  $I_{1608}$  and  $C_{\text{PCB-77}}$ . The error bar was obtained by three replicate determinations.

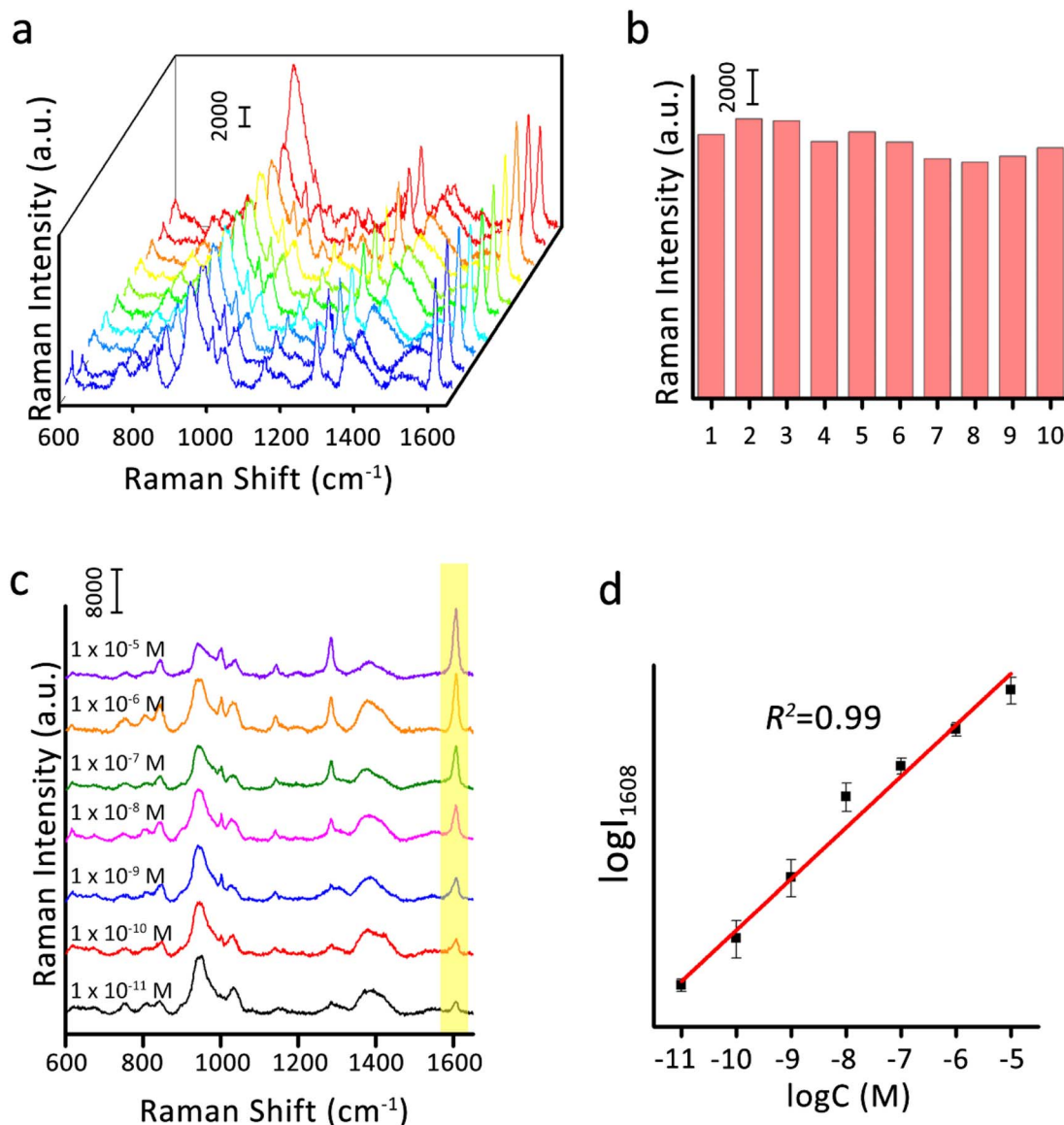


Fig. 7 (a) The Raman spectra on the C-NR@Ag substrate at 10 points based on Fig. S11.† (b) The peak intensity of  $1650\text{ cm}^{-1}$  based on (a). (c)  $10^{-5}$  to  $10^{-11}$  M concentrations of PCB-77 are detected on the C-NR@Ag substrate. (d) Correlation between the log-log plot of  $I_{1608}$  and  $C_{\text{PCB-77}}$ . The error bar was obtained by three replicate determinations.

## Conclusions

In summary, the C-NR@Ag substrate has been fabricated by the RIE method, MACE method, and galvanic deposition subsequently for SERS detection of PCB-77. By adjusting the process of MACE and deposition time of the galvanic cell, the C-NR@Ag substrate could be finely controlled and fabricated. Ag-nanoplates are uniformly assembled on the C-NR structure generating hot spots and enhancing Raman signals. The EF of the substrate for R6G is  $3.6 \times 10^6$ , and a concentration of  $1.0 \times 10^{-12}$  M for PCB-77 can be detected, which shows the sensitivity of the substrate. The enhanced sensitivity enables the detection of PCB-77 at the concentration as low as  $1.0 \times 10^{-12}$  M, indicating the high sensitivity of the substrate. Additionally, due to

the semi-volatile nature of PCB-77, the C-NR@Ag substrate enables trace detection of it at concentration levels as low as  $1.0 \times 10^{-11}$  M by non-contact collection. This study lays the foundation for on-site detection of PCB-77 and provides a promising approach to enhance the performance of SERS substrates.

## Data availability

The data supporting this article have been included as part of the ESI.†

## Author contributions

Jinran Chen: conceptualization, methodology, investigation, data curation, and writing – original draft. Xiurui Ke: writing –

original draft. Zhou Zhou: investigation. Wenqi Ye: writing – review & editing. Hong Liu: review & editing. Wei Zhang: funding acquisition, review & editing. Xiaohong Liu: funding acquisition, writing – review & editing.

## Conflicts of interest

There are no conflicts to declare.

## Acknowledgements

The authors gratefully acknowledge financial support from the National Natural Science Foundation of China (grant no. 62175237), Interdiscipline Team Project under auspices of “Light of West” Program in Chinese Academy of Sciences (grant no. xzbz-zdsys-202106), Young Scholar of Regional Development Program in Chinese Academy of Sciences (grant no. 2021), The Natural Science Foundation of Chongqing, China (grant no. CSTB2023NSCQ-MSX0768), Chongqing Water Science and Technology Project (grant no. CQSLK-2022006), and Three Gorges follow-up project (grant no. CQS23C00400). During the preparation of this work the authors used AI-assisted technologies in order to polish the language.

## References

- B. Sun, Q. Li, M. Zheng, G. Su, S. Lin, M. Wu, C. Li, Q. Wang, Y. Tao, L. Dai, Y. Qin and B. Meng, *Environ. Pollut.*, 2020, **265**, 114908.
- K. Magulova and A. Priceputu, *Environ. Pollut.*, 2016, **217**, 82–84.
- L. R. Bordajandi, J. J. Ramos, J. Sanz, M. J. Gonzalez and L. Ramos, *J. Chromatogr. A*, 2008, **1186**, 312–324.
- H. Wang, A. Adamcakova-Dodd, S. Flor, L. Gosse, V. E. Klenov, J. M. Stolwijk, H.-J. Lehmler, K. C. Hornbuckle, G. Ludewig, L. W. Robertson and P. S. Thorne, *Environ. Sci. Technol.*, 2020, **54**, 15976–15985.
- D. Zhang, P. Saktrakulkla, K. Tuttle, R. F. Marek, H.-J. Lehmler, K. Wang, K. C. Hornbuckle and M. W. Duffel, *Environ. Sci. Technol.*, 2021, **55**, 2473–2481.
- L. Fang, X. Liao, B. Jia, L. Shi, L. Kang, L. Zhou and W. Kong, *Biosens. Bioelectron.*, 2020, **164**, 112255.
- S. Alsefiri, T. Balbaied and E. Moore, *Chemosensors*, 2021, **9**, 307.
- Y. Shao, H. Zhou, Q. Wu, Y. Xiong, J. Wang and Y. Ding, *Biotechnol. Adv.*, 2021, **53**, 107867.
- D. Huang, Z. Zhuang, Z. Wang, S. Li, H. Zhong, Z. Liu, Z. Guo and W. Zhang, *Appl. Surf. Sci.*, 2019, **497**, 143825.
- P. Bruce-Vanderpuije, D. Megson, E. J. Reiner, L. Bradley, S. Adu-Kumi and J. A. Gardella Jr, *Environ. Pollut.*, 2019, **245**, 331–342.
- X. Cao, S. Huo, H. Zhang, J. Zheng, Z. He, C. Ma and S. Song, *J. Environ. Sci.*, 2021, **109**, 15–25.
- R. A. Hites, *Anal. Chem.*, 2016, **88**, 6955–6961.
- J. Niu, L. Jiang, L. Nie, J. Liao, L. Bu, G. Dong, D. Song, G. Tang and Q. Zhou, *Food Chem.*, 2025, **464**, 141655.
- L. Su, G. Wang, L. Zhao, Y. Deng, Y. Guo, Y. Xiao, H. Wang, C. Dong and L. Fan, *Sci. Total Environ.*, 2024, **946**, 173982.
- Y. Liu, S. Qiao, C. Fang, Y. He, H. Sun, J. Liu and Y. Ma, *Opto-Electron. Adv.*, 2024, **7**, 230230.
- J. Cheng, P. L. Wang and X. O. Su, *TrAC, Trends Anal. Chem.*, 2020, **125**, 115836.
- H. Chen, C. Han, L. Zhang and Y. Wu, *Nanotechnology*, 2024, **35**, 195710.
- S. Luo, A. Mancini, F. Wang, J. Liu, S. A. Maier and J. C. de Mello, *ACS Nano*, 2022, **16**, 7438–7447.
- C. Li, H. Wang, Y. Luo, G. Wen and Z. Jiang, *Food Chem.*, 2019, **289**, 531–536.
- A. González Fà, F. Pignanelli, I. López-Corral, R. Faccio, A. Juan and M. S. Di Nezio, *TrAC, Trends Anal. Chem.*, 2019, **121**, 115673.
- B. Tim, P. Błaszczewicz, A. B. Nowicka and M. Kotkowiak, *Appl. Surf. Sci.*, 2022, **573**, 151518.
- Y. Wu, T. Sun, M. Shao, C. Ji, C. Li, C. Zhang and Z. Li, *Laser Photonics Rev.*, 2024, 2401152.
- M. Shao, C. Ji, J. Tan, B. Du, X. Zhao, J. Yu, B. Man, K. Xu, C. Zhang and Z. Li, *Opto-Electron. Adv.*, 2023, **6**, 230094.
- Z. Huang, G. Meng, Q. Huang, B. Chen, C. Zhu and Z. Zhang, *J. Raman Spectrosc.*, 2012, **44**, 240–246.
- Y. Liu, X. Li, J. Cheng, N. Zhou, L. Zhang, H. Mao and C. Huang, *J. Innovative Opt. Health Sci.*, 2021, **14**, 2141005.
- S. Jiang, L. Chang, J. Luo, J. Zhang, X. Liu, C. Y. Lee and W. Zhang, *Analyst*, 2021, **146**, 6170–6177.
- T. Wu, K. Li, N. Zhang, J. Xia, Q. Zeng, X. Wen, U. S. Dinis, M. Olivo, Z. Shen, Z. Liu, Q. Xiong, Y. Luo, S. A. Maier and L. Wei, *Adv. Opt. Mater.*, 2019, **7**, 1900905.
- Q. Wang, J. Li, Y. Song, L. Duan, C. Yan, L. Qu, Y. Wu and C. Han, *J. Hazard. Mater.*, 2022, **426**, 128085.
- H. Tang, G. Meng, Q. Huang, Z. Zhang, Z. Huang and C. Zhu, *Adv. Funct. Mater.*, 2012, **22**, 218–224.
- L. Chang, S. Jiang, J. Luo, J. Zhang, X. Liu, C.-Y. Lee and W. Zhang, *Environ. Sci.: Nano*, 2022, **9**, 542–553.
- Z. Li, K. Sun, Z. Du, B. Chen and X. He, *Nanomaterials*, 2018, **8**, 265.
- C. Zhu, Q. Zhao, D. Huo, X. Hu and X. Wang, *Mater. Chem. Phys.*, 2021, **263**, 124388.
- M. Sajitha, B. Abraham, R. B. Nelliyil and K. Yoosaf, *ACS Appl. Nano Mater.*, 2021, **4**, 10038–10046.
- Z. Li, G. Meng, Q. Huang, C. Zhu, Z. Zhang and X. Li, *Chem*, 2012, **18**, 14948–14953.
- S. Yang, D. Slotcavage, J. D. Mai, F. Guo, S. Li, Y. Zhao, Y. Lei, C. E. Cameron and T. J. Huang, *J. Mater. Chem. C*, 2014, **2**, 8350–8356.
- H. Tang, G. Meng, Q. Huang, Z. Zhang, Z. Huang and C. Zhu, *Adv. Funct. Mater.*, 2011, **22**, 218–224.
- C. Zhu, G. Meng, Q. Huang and Z. Huang, *J. Hazard. Mater.*, 2011, **211**, 389–395.
- Z. Li, Z. Du, K. Sun, X. He and B. Chen, *RSC Adv.*, 2017, **7**, 53157–53163.

- 39 C. F. Tan, S. A. Azmansah, H. Zhu, Q. H. Xu and G. W. Ho, *Adv. Mater.*, 2017, **29**, 1604417.
- 40 L. Chang, X. Liu, J. Luo, C. Y. Lee, J. Zhang, X. Fan and W. Zhang, *Adv. Mater.*, 2024, **36**, 2310469.
- 41 C. H. Hsu, S. M. Liu, S. Y. Lien, X. Y. Zhang, Y. S. Cho, Y. H. Huang, S. Zhang, S. Y. Chen and W. Z. Zhu, *Nanomaterials*, 2019, **9**, 1392.
- 42 K. Sun, Q. Huang, G. Meng and Y. Lu, *ACS Appl. Mater. Interfaces*, 2016, **8**, 5723–5728.
- 43 Y. Lai, W. Pan, S. Ni, D. Zhang and J. Zhan, *Chemosphere*, 2011, **85**, 412–417.